

MOSformer: Momentum Encoder-based Inter-slice Fusion Transformer for Medical Image Segmentation

De-Xing Huang^{1,2}, Xiao-Hu Zhou^{1,2*}, Mei-Jiang Gui^{1,2}, Xiao-Liang Xie^{1,2}, Shi-Qi Liu^{1,2}, Shuang-Yi Wang^{1,2}, Zhen-Qiu Feng^{1,2}, and Zeng-Guang Hou^{1,2*}

¹The State Key Laboratory of Multimodal Artificial Intelligence Systems, Institute of Automation, Chinese Academy of Sciences, Beijing, China.

²The School of Artificial Intelligence, University of Chinese Academy of Sciences, Beijing, China.

*Address correspondence to: {xiaohu.zhou, zengguang.hou}@ia.ac.cn

Abstract

Medical image segmentation takes an important position in various clinical applications. 2.5D-based segmentation models bridge the computational efficiency of 2D-based models with the spatial perception capabilities of 3D-based models. However, existing 2.5D-based models primarily adopt a single encoder to extract features of target and neighborhood slices, failing to effectively fuse inter-slice information, resulting in suboptimal segmentation performance. In this study, a novel momentum encoder-based inter-slice fusion transformer (**MOSformer**) is proposed to overcome this issue by leveraging inter-slice information at multi-scale feature maps extracted by different encoders. Specifically, dual encoders are employed to enhance feature distinguishability among different slices. One of the encoders is moving-averaged to maintain consistent slice representations. Moreover, an inter-slice fusion transformer (IF-Trans) module is developed to fuse inter-slice multi-scale features. The **MOSformer** is evaluated on three benchmark datasets (Synapse, ACDC, and AMOS), achieving a new state-of-the-art with 85.63%, 92.19%, and 85.43% DSC, respectively. These results demonstrate **MOSformer**'s competitiveness in medical image segmentation.

1 Introduction

Medical image segmentation plays a crucial role in numerous clinical applications, such as computer-aided diagnoses [1], image-guided interventions [2], [3], [4], and surgical robotics [5], [6], [7]. UNet [8] and its variants [9], [10], [11] have been widely used in this field, achieving tremendous success in different medical imaging modalities. However, accurate and efficient segmentation of 3D medical images still remains a non-trivial task [12].

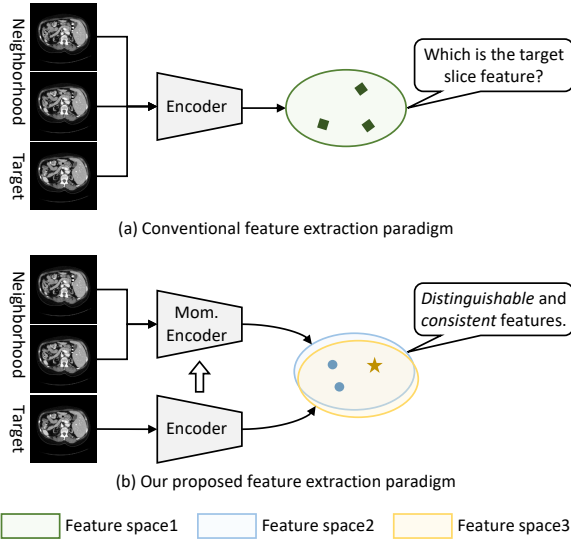


Figure 1: Comparison between conventional feature extraction paradigm of 2.5D-based segmentation models and our proposed paradigm. (a) Conventional approaches use a single encoder to extract features of all slices. Therefore, target slices and neighborhood slices share the same feature space. (b) Our proposed paradigm adopts dual encoders to extract features of target and neighborhood slices, respectively. Momentum update is used in the neighborhood slice encoder. Hence, feature spaces of target and neighborhood slices are distinguishable and consistent. (Mom.: Momentum.)

Current mainstream segmentation methods can be classified into two categories: 2D-based and 3D-based methods [13]. 2D-based methods split 3D images into 2D slices and segment them individually, while 3D-based methods divide 3D images into smaller patches and then segment these patches individually. Despite impressive performance achieved by state-of-the-art methods [14], they still exhibit some limitations. Most 2D-based methods focus on architecture design to enhance intra-slice representations for better performance, such as incorporating attention modules [15], [16] or adopting transformers [17], [18]. However, these methods overlook inter-slice cues, which is also crucial for accurate segmentation. In contrast, 3D-based methods can capture intra- and inter-slice information for segmentation but demand substantial GPU memory and computational resources. Additionally, they tend to perform poorly in images with anisotropic voxel spacing since they are primarily designed for 3D images with nearly isotropic voxel spacing [19], [20].

In order to combine advantages of 2D-based and 3D-based methods, some studies have been done to explore 2.5D-based segmentation models [13]. The main idea of these methods is to fuse inter-slice (neighborhood slices) information into 2D-based models when segment specific slices (target slices). The most direct way to achieve inter-slice fusion is by concatenating slices as multi-channel inputs. However, it is inefficient, making models challenging to extract useful features for target slices [13]. Therefore, some studies focus on exploring “smart” ways of inter-slice fusion. Most of them formulate 2D slices as time sequences and adopt recurrent neural network (RNN) [21], transformers [22], [23] or attention mechanisms [24] to fuse inter-slice information.

While current 2.5D-based methods have achieved impressive segmentation results, they struggle

with distinguishing individual slices during inter-slice fusion, and consequently fail to learn reliable inter-slice representations essential for accurate segmentation [13]. The root of this problem lies in the use of a single encoder to process all input slices, resulting in the same feature distributions across the feature space, as shown in Fig. 1 (a). For example, the features of the i -th slice remain identical whether it is considered as the target slice or the neighboring slice. This indistinguishability becomes problematic in scenarios where consecutive slices, such as the i -th and the $(i+1)$ -th, are target slices, respectively. Models fail to differentiate the i -th slice’s features as belonging to the target or the neighboring slice, thereby hampering the extraction of valuable inter-slice information for segmentation.

To address the above issue, a novel 2.5D-based segmentation model, **MOSformer**, **M**omentum encoder-based inter-**S**lice fusion **transformer** is proposed to effectively leverage inter-slice information for 3D medical image segmentation. **MOSformer** follows the design of the U-shape architecture [8]. In order to enhance feature distinguishability of each slice, dual encoders are utilized in our model. One for target slices and the other for neighborhood slices. Parameters of the target slice encoder are updated by back-propagation, and parameters of the neighborhood slice encoder are updated using a momentum update. Therefore, features can remain distinguishable and consistent, promoting inter-slice fusion, as shown in Fig. 1 (b). Furthermore, an efficient inter-slice fusion transformer (IF-Trans) module is proposed to capture inter-slice cues at multi-scale feature maps based on **Swin transformer** [25].

The main contributions of this work are summarized as follows:

- A novel 2.5D-based model **MOSformer** is proposed to fully exploit inter-slice information for 3D medical image segmentation.
- To make slice features distinguishable and consistent, dual encoders with a momentum update are introduced. Moreover, the inter-slice fusion transformer (IF-Trans) module is developed to efficiently fuse inter-slice information.
- State-of-the-art segmentation performance has been achieved by our model on three benchmark datasets, including Synapse, ACDC, and AMOS.

The remainder of this paper is organized as follows: Section 2 briefly reviews current segmentation methods. Section 3 depicts the proposed model in detail. Section 4 introduces model configurations and datasets. The experimental results are presented in Section 5. Finally, Section 6 concludes this article.

2 Related Works

2.1 2.5D-based Medical Image Segmentation

Several 2.5D-based approaches have been proposed for efficient medical image segmentation by leveraging inter-slice information. Early methods concatenated multiple consecutive 2D slices into a multi-channel input and adopted 2D-based models to segment specific regions of the middle

slice [26], [27]. However, 2D multi-channel inputs make models difficult to extract information of individual information [13], limiting the potential of 2.5D-based model. To solve the above problem, some works treated continuous 2D slices as temporal sequences and utilized recurrent neural networks (RNNs) [21], [28] to learn inter-slice information. For example, Chen *et al.* [21] suggested a 2.5D segmentation framework combining with k -UNet and bi-directional convolutional LSTM (BDC-LSTM) to integrate inter-slice information. Although RNNs can help improve the performance of 2.5D-based models to some extent, training costs of these methods are considerably high [29]. Instead of RNNs, recent studies utilized attention mechanisms or transformers to fuse inter-slice information at feature level effectively. Zhang *et al.* [24] proposed an attention fusion module to refine segmentation results by fusing the information of adjacent slices. Li *et al.* [30] adopted a 2.5D coarse-to-fine architecture, which benefits from the inter-slice context knowledge from consistency context similarity and discrepancy context. Guo *et al.* [31] adopted 2D UNet as the backbone and fused inter-slice information via a transformer at the bottom layer of the encoder. Yan *et al.* [22] proposed AFTer-UNet with an axial fusion mechanism based on transformer to fuse intra- and inter-slice contextual information. Hung *et al.* [23], [32] introduced novel cross-slice attention mechanisms based on transformer to learn cross-slice information at multiple scales. However, the aforementioned methods fail to capture useful inter-slice information for the target slice which needed to be segmented, since they use a single encoder to extract slice features, making models difficult to distinct target slices and neighborhood slices [13].

Different from previous works, we adopt dual encoders with a momentum update to extract features of target slices and neighborhood slices, respectively. We demonstrate such design can make features of target slices and neighborhood slices distinguishable and consistent, further boosting inter-slice fusion.

2.2 Transformers in Medical Image Segmentation

Recently, with the tremendous success of vision transformer (ViT) [33] in various computer vision tasks [34], [35], many works have explored using transformers in medical image segmentation. Compared with CNNs, transformers can capture long-range dependencies by sequence modeling and multihead self-attention (MHSA) [33], achieving better segmentation performance. Chen *et al.* [18] proposed TransUNet, combining UNet [8] and transformer, where transformer encodes feature maps from CNN encoder to extract global contexts for the decoder to generate segmentation results. Cao *et al.* [17] are the first to employ a pure transformer architecture for medical image segmentation. Convolutional layers in UNet are all replaced by blocks in Swin transformer [25]. However, this architecture does not obtain better performance [36]. Huang *et al.* introduced MISSformer [37], which incorporates an encoder-decoder architecture built on enhanced transformer blocks. These blocks are connected through the ReMixed transformer context bridge, enhancing the model’s ability to capture discriminative details. You *et al.* [36] presented CASTformer with a class-aware transformer module to better capture discriminative regions of target objects. Moreover, they utilized adversarial learning to boost segmentation accuracies. However, the 2D-based methods mentioned above face limitations in leveraging inter-slice information, which hinders their potential for further perfor-

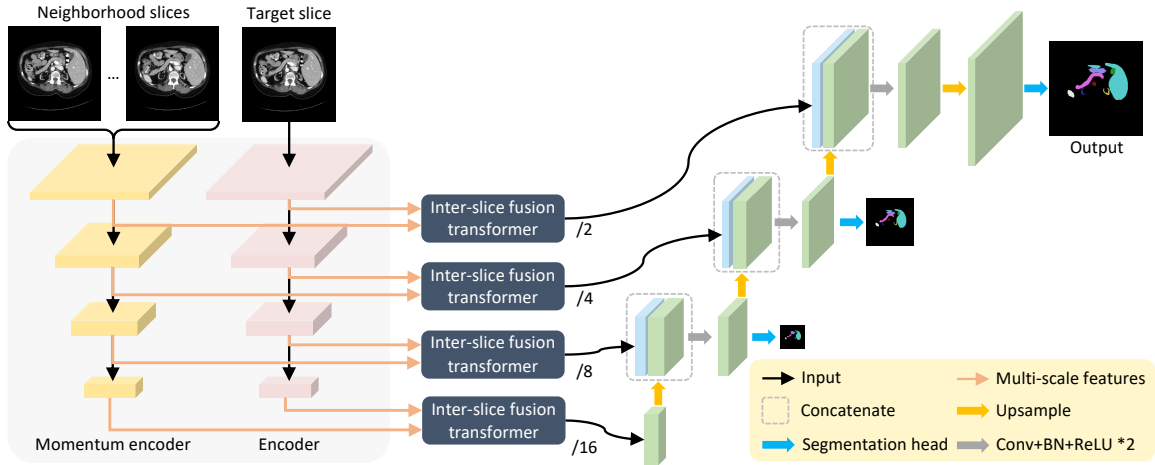


Figure 2: The architecture of **MOSformer**. It consists of dual encoders: the momentum encoder for extracting neighborhood slice features and the encoder for extracting target slice features. The IF-Trans is designed to achieve inter-slice fusion at multi-scale features. After that, fused features are fed to the CNN decoder to generate segmentation maps of target slices.

mance improvements. Some attempts have been made to build 3D-based transformer segmentation models. UNETR [38] pioneered the use of a transformer-based encoder to learn global contexts from volumetric data. CoTr [39] introduced a deformable self-attention mechanism to reduce computational complexity. However, simplifying self-attention may cause contextual information loss [22]. nnFormer [40] is an interleave architecture, where convolution layers encode precise spatial information and transformer layers fully explore global dependencies. Similar to Swin transformer [25], a computationally-efficient way to calculate self-attention is proposed in nnFormer.

In this work, we proposed a inter-slice fusion transformer module based on Swin transformer [25] to effectively fuse inter-slice information. Unlike current methods only use transformer to learn intra-slice contexts, we extent self-attention of transformers to explore both intra- and inter-slice cues.

3 Method

3.1 Overall Architecture

The detailed architecture of **MOSformer** is shown in Fig. 2. Like most previous works for medical image segmentation, we utilize a hybrid encoder-decoder architecture, combining the advantages of CNNs and transformers [40]. $\mathbf{x}_i \in \mathbb{R}^{C \times H \times W}$ is the input of the encoder and represents the target slice for segmentation, where i indicates the i -th slice of a 3D volume $\mathbf{X} \in \mathbb{R}^{C \times H \times W \times D}$, where C , H , W , and D denote the channel, height, width, and depth of \mathbf{X} . $\mathbf{x}_j \in \mathbb{R}^{C \times H \times W}$ are inputs of the momentum encoder and represent neighborhood slices of \mathbf{x}_i , $j \in [i - s, i + s] / \{i\}$ and s represents the s -th neighborhood of \mathbf{x}_i . Finally, the model generates the segmentation map $\mathbf{y}_i \in \mathbb{R}^{C_0 \times H \times W}$ of \mathbf{x}_i , where C_0 is the number of label classes.

We utilize ResNet50 [41] as our encoder to extract multi-scale features of input slices. Dual

encoders with a momentum update are adopted in **MOSformer** to strengthen feature distinguishability and maintain feature consistency. Furthermore, IF-Trans modules are used at multi-scale (1/2, 1/4, 1/8, and 1/16) to fuse inter-slice features extracted by dual encoders. Then the fused features are sent to the decoder via skip connections. The final segmentation predictions are derived via a segmentation head (1×1 convolutional layer).

3.2 Dual Encoders with A Momentum Update

Conventional 2.5D-based methods utilize a single encoder to process all input slices and then fuse inter-slice information at feature level. This may make models challenging to distinguish each slice [13] since they are from the same feature space, as illustrated in Fig. 1 (a). Models cannot focus on capturing discriminative inter-slice representations for target slices. A simple idea is to use two independently updated encoders to process neighborhood slices and target slices, respectively. However, this approach achieves suboptimal performance in experiments conducted in Section 5.2. We hypothesize that such unsatisfactory performance is caused by two independently update encoders that reduce slice features' consistency which is also crucial for inter-slice fusion.

Inspired by [42], a momentum update approach is adopted to overcome the above issue. Parameters of target slice encoder θ_1 are updated by standard back-propagation. Parameters of neighborhood slice encoder θ_2 are updated by:

$$\theta_2 \leftarrow m * \theta_2 + (1 - m) * \theta_1 \quad (1)$$

where $m \in [0, 1]$ is a momentum coefficient (0.1 in default). We investigate the effect of m in Section 5.3 and conclude that m should be relatively small to make features consistent. Under this circumstance, slice features are distinguishable and consistent, as shown in Fig. 1 (b) and Fig. 7 (c), facilitating the model in effectively capturing inter-slice information.

3.3 Inter-slice Fusion Transformer

In this section, inter-slice fusion transformer (IF-Trans) is proposed to capture inter-slice cues, as shown in Fig. 3. We utilize IF-Trans at multi-scales and discuss the benefit of multi-scale learning in Section 5.3. Inputs of the k -th IF-Trans are feature maps $\{f_{i-s}^k, \dots, f_i^k, \dots, f_{i+s}^k\}$ extracted by the encoder and the momentum encoder, where k represents the k -st scale of two encoders ($k = 1, 2, 3, 4$). The neighborhood slice number s is set to 1 in our default configuration. We give a detailed analysis of s in Section 5.3. Therefore, the model uses adjacent (1-th neighborhood) slices of the target slice x_i as additional inputs.

Different from standard self-attention [43] with quadratic complexity, the proposed IF-Trans only calculates self-attention within the local window. As shown in the left part of Fig. 3, feature maps are portioned to several non-overlapping windows¹. Compared with **Swin transformer** [25], we compute self-attention within inter- and intra-slice local windows (*i.e.*, CSW-MSA, cross-slice window-based multi-head self-attention) instead of intra-slice local windows. Therefore, the orange

¹For intuitive explanation, feature maps are replaced by input images, and the number of pixels is simplified to 16.

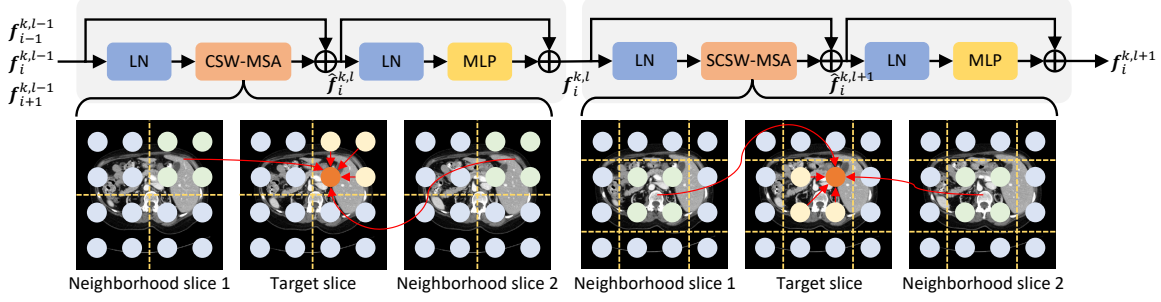


Figure 3: Schematic of inter-slice fusion transformer (IF-Trans) module. The neighborhood slice number is set to 1 in this figure, consistent with our default model configuration. It has two successive IF-Trans with different window partitioning configurations. The window-based self-attention is expanded to the inter-slice dimension, promoting target slice pixels to learn intra- and inter-slice contexts.

pixel in the target slice can capture not only intra-slice information (yellow pixels) but also perceives inter-slice information (green pixels).

However, the local CSW-MSA lacks connections across windows, degrading its feature formulation power. Similar to [25], a shifted window partitioning strategy is introduced, allowing each pixel to receive broader views from intra- and inter-slices. In Fig. 3, the first transformer module adopts a regular window partition approach, and the feature map is evenly divided into 2×2 windows of size 2×2 ($M = 2$)². The second transformer module uses a different partitioning configuration. Windows of the preceding layer are displaced by $(\lfloor \frac{M}{2} \rfloor, \lfloor \frac{M}{2} \rfloor)$ pixels to generate new windows. By doing so, the orange pixel can conduct self-attention (*i.e.*, SCSW-MSA, a shifted version of CSW-MSA) with more pixels, boosting representation abilities. In practice, these two configurations are served as two consecutive layers to get an IF-Trans module. Outputs of IF-Trans can be formulated as:

$$\begin{aligned} \hat{f}_i^{k,l} &= \mathcal{T} \left\{ \text{LN} \left(f_{i-1}^{k,l-1} \right), \text{LN} \left(f_i^{k,l-1} \right), \text{LN} \left(f_{i+1}^{k,l-1} \right) \right\} + f_i^{k,l-1} \\ f_i^{k,l} &= \mathcal{M} \left\{ \text{LN} \left(\hat{f}_i^{k,l} \right) \right\} + \hat{f}_i^{k,l} \\ \hat{f}_i^{k,l+1} &= \mathcal{T}^S \left\{ \text{LN} \left(f_{i-1}^{k,l} \right), \text{LN} \left(f_i^{k,l} \right), \text{LN} \left(f_{i+1}^{k,l} \right) \right\} + f_i^{k,l} \\ f_i^{k,l+1} &= \mathcal{M} \left\{ \text{LN} \left(\hat{f}_i^{k,l+1} \right) \right\} + \hat{f}_i^{k,l+1} \end{aligned} \quad (2)$$

where $\hat{f}_i^{k,l}$ and $f_i^{k,l}$ represents output feature maps of the (S)CSW-MSA module $\mathcal{T}^{(S)}$ and the multi-layer perceptron (MLP) module \mathcal{M} in the l -th layer, respectively. LN indicates layer normalization. The query-key-value (QKV) self-attrntion [43] in (S)CSW-MSA is computed as follows:

$$\text{Attention}(\mathbf{Q}, \mathbf{K}, \mathbf{V}) = \text{Softmax} \left(\frac{\mathbf{Q} \mathbf{K}^T}{\sqrt{d}} + \mathbf{B} \right) \mathbf{V} \quad (3)$$

where $\mathbf{Q} \in \mathbb{R}^{\{M^2*(2*s+1)\} \times d}$, $\mathbf{K} \in \mathbb{R}^{\{M^2*(2*s+1)\} \times d}$, and $\mathbf{V} \in \mathbb{R}^{\{M^2*(2*s+1)\} \times d_0}$ denote query, key,

²To correspond with Fig. 3, M is set to 2 here.

and value matrices. d and d_0 are embedding dimensions of query/key and value. In practice, d is equal to d_0 . \mathbf{B} represents the position embedding matrix, and values are taken from the bias matrix $\hat{\mathbf{B}} \in \mathbb{R}^{(2M-1) \times (2M-1)}$.

3.4 Loss Function

Following previous methods [39], [38], [40], our model is trained end-to-end using the deep supervision strategy [44]. As illustrated in Fig. 2, final segmentation results are generated by the segmentation head (1×1 convolutional layer). Additionally, two smaller resolutions of decoder outputs are selected as auxiliary supervision signals. The deep supervision path in Fig. 2 consists of an upsample layer and a 1×1 convolutional layer. Therefore, the loss function can be formulated as follows:

$$\mathcal{L}_{\text{seg}} = \lambda_1 \mathcal{L}_{\{H, W\}} + \lambda_2 \mathcal{L}_{\{\frac{H}{2}, \frac{W}{2}\}} + \lambda_3 \mathcal{L}_{\{\frac{H}{4}, \frac{W}{4}\}} \quad (4)$$

where λ_1 , λ_2 , and λ_3 are $\frac{1}{2}$, $\frac{1}{4}$, and $\frac{1}{8}$, respectively. $\mathcal{L}_{\{h, w\}}$ represents the loss function on $h \times w$ resolution. It is a linear combination of cross-entropy loss \mathcal{L}_{CE} and Dice loss \mathcal{L}_{DSC} :

$$\mathcal{L}_{\{h, w\}} = \alpha_1 \mathcal{L}_{\text{CE}} + \alpha_2 \mathcal{L}_{\text{DSC}} \quad (5)$$

where α_1 and α_2 are 0.8 and 1.2, respectively.

4 Experimental Setup

4.1 Datasets

To thoroughly compare `M0Sformer` to previous methods, we conduct experiments on three challenging benchmarks: the Synapse multi-organ segmentation dataset [45], the automated cardiac diagnosis challenge (ACDC) dataset [46], and the abdominal organ segmentation (AMOS) dataset [47].

Synapse for Multi-organ Segmentation. This dataset consists of 30 abdominal CT scans with 8 organs (*aorta*, *gallbladder*, *left kidney*, *right kidney*, *liver*, *pancreas*, *spleen*, and *stomach*). Each volume has $85 \sim 198$ slices of 512×512 pixels. Following the splits adopted in `TransUNet` [18], the dataset is divided into 18 training cases and 12 testing cases.

ACDC for Automated Cardiac Diagnosis Challenge. The ACDC dataset includes cardiac MRI images of 100 patients from real clinical exams with manual annotations of *left ventricle* (LV), *right ventricle* (RV), and *myocardium* (Myo). Consistent with `TransUNet` [18], the dataset is split into 70 training cases, 10 validation cases, and 20 testing cases.

AMOS for Abdominal Organ Segmentation. The AMOS dataset is a comprehensive abdominal organ segmentation dataset that includes patient annotations of 15 abdominal organs (*aorta*, *bladder*, *duodenum*, *esophagus*, *gallbladder*, *inferior vena cava*, *left adrenal gland*, *left kidney*, *liver*, *pancreas*, *prostate/uterus*, *right adrenal gland*, *right kidney*, *spleen*, and *stomach*) from different centers, modalities, scanners, phases, and diseases. Only CT scans are utilized in our experiments,

consisting of 200 training cases and 100 testing cases.

4.2 Implementation Details

All experiments are implemented based on PyTorch 1.12.0, Python 3.8, and Ubuntu 18.04. Our model is trained on a single Nvidia A6000 GPU with 48GB of memory. The same model configurations are utilized on three datasets. Input medical images are resized to 224×224 for fair comparison. SGD optimizer with momentum of 0.9 and weight decay of $1e^{-4}$ is adopted to train our model for 300 epochs. The batch size is set to 24. A cosine learning rate scheduler with five epochs of linear warm-up is used during training, and the maximum and minimum learning rates are $3e^{-2}$ and $5e^{-3}$, respectively.

4.3 Evaluation Metrics

Two metrics are utilized to evaluate segmentation performance of models: Dice similarity score (DSC), and 95% Hausdorff distance (HD95).

DSC is utilized to evaluate overlaps between ground truths and segmentation results and is defined as follows:

$$\text{DSC}(P, G) = 2 \times \frac{|P \cap G|}{|P| + |G|} \quad (6)$$

where P refers to model predictions and G refers to ground truths.

HD95 is adopted to measure the 95% distance between boundaries of model predictions and ground truths. It is defined as follows:

$$\text{HD}_{95} = \max \{d_{PG}, d_{GP}\} \quad (7)$$

where d_{PG} is the maximum 95% distance between model predictions and ground truths. d_{GP} is the maximum 95% distance between ground truths and model predictions.

5 Results

5.1 Comparisons with SOTAs

Multi-organ Segmentation (Synapse). Quantitative results of state-of-the-art models and our **MOSformer** are presented in Table 1. **MOSformer** achieves 85.63% DSC and 13.40 mm HD95 on this dataset. Compared with the best 2D-based methods, *i.e.*, **CASTformer** [36], **MOSformer** is able to surpass it by a large margin (+3.08% DSC and -9.33 mm HD95). For 2.5D-based baselines, **MOSformer** demonstrates notable performance enhances, offers at least +4.61% and +1.39% DSC gains over **AFTer-UNet** [22] and **TransUNet-2.5D** [54]. These results indicate **i**) the necessity of inter-slice information in 3D medical image segmentation; and **ii**) the effectiveness of distinguishable and consistent slice features produces by dual encoders with a momentum update.

Table 1: Comparison with state-of-the-art models on the multi-organ segmentation (Synapse) dataset. The best results are highlighted in **blue** and the second-best results are highlighted in **red**. The evaluation metrics are DSC and HD95, consisting with TransUNet [18]. Moreover, DSC of each organ is reported in this table. \dagger means the results are borrowed from [40].

Dimension	Method	Average		Atria	Gallbladder	Kidney (L)	Kidney (R)	Liver	Pancreas	Spleen	Stomach
		DSC (%) \uparrow	HD95 (mm) \downarrow								
2D	UNet [8] [MICCAI'15]	76.85	39.70	89.07	69.72	77.77	68.60	93.43	53.98	86.67	75.58
	AttnUNet [48] [MedIA'19]	77.77	36.02	89.55	68.88	77.98	71.11	93.57	58.04	87.30	75.75
	TransUNet [18] [MedIA'24]	77.48	31.69	87.23	63.13	81.87	77.02	94.08	55.86	85.08	75.62
	MISSFormer [37] [TMI'23]	81.96	18.20	86.99	68.65	85.21	82.00	94.41	65.67	91.92	80.81
	SwinUNet [17] [ICCVW'22]	79.12	21.55	85.47	66.53	83.28	79.61	94.29	56.58	90.66	76.60
	MT-UNet [49] [ICASSP'22]	78.59	26.59	87.92	64.99	81.47	77.29	93.06	59.46	87.75	76.81
	UCTransNet [50] [AAAI'22]	78.23	26.75	88.86	66.97	80.19	73.18	93.17	56.22	87.84	79.43
	CASTformer [36] [NeurIPS'22]	82.55	22.73	89.05	67.48	86.05	82.17	95.61	67.49	91.00	81.55
3D	HiFormer [51] [WACV'23]	80.39	14.70	86.21	65.69	85.23	79.77	94.61	59.52	90.99	81.08
	V-Net [52] [BDV'16]	68.81	-	75.34	51.87	77.10	80.75	87.84	40.05	80.56	56.98
	CoTr \dagger [39] [MICCAI'21]	80.78	19.15	85.42	68.93	85.45	83.62	93.89	63.77	88.58	76.23
	UNETR \dagger [38] [WACV'22]	79.56	22.97	89.99	60.56	85.66	84.80	94.46	59.25	87.81	73.99
2.5D	SwinUNETR \dagger [53] [MICCAI'22]	83.51	14.78	90.75	66.72	86.51	85.88	95.33	70.07	94.59	78.20
	nnFormer [40] [TIP'23]	86.57	10.63	92.04	70.17	86.57	86.25	96.84	83.35	90.51	86.83
	AFTer-UNet [22] [WACV'22]	81.02	-	90.91	64.81	87.90	85.30	92.20	63.54	90.99	72.48
2.5D	TransUNet-2.5D [54] [TIP'23]	84.24	19.24	89.97	73.28	83.99	81.33	95.61	70.39	94.59	84.78
	MOSformer [ours]	85.63	13.40	88.95	71.90	90.32	83.58	95.96	74.14	92.29	87.87

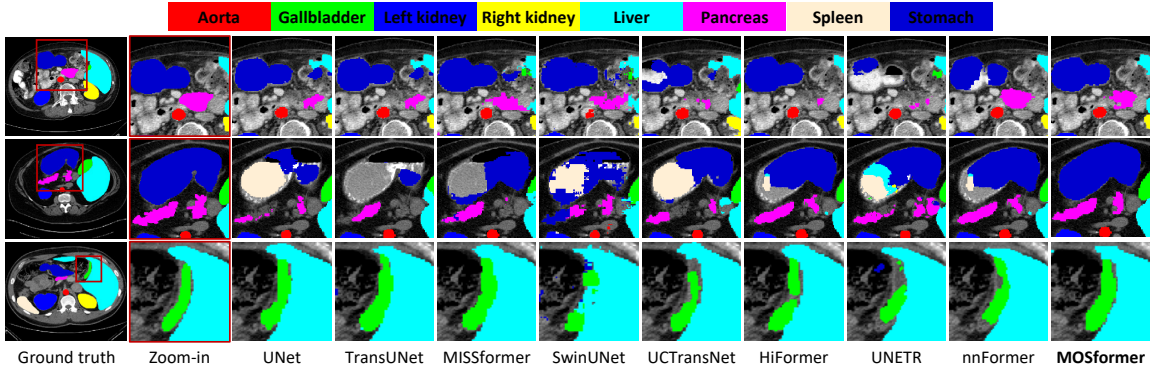


Figure 4: Visual comparisons with current state-of-the-art methods on the multi-organ segmentation (Synapse) dataset.

We also compare **MOSformer** with 3D-based segmentation methods. **MOSformer** still has competitive performance, surpassing four of the most widely recognized models and achieving comparable performance to **nnFormer** [40]. It should be noted that **MOSformer** obtains better DSC than **nnFormer** in four organs (half of the categories), including *gallbladder* (+1.73%), *left kidney* (+3.75%), *spleen* (+1.78%), and *stomach* (+1.04%). Among these organs, *gallbladder* and *stomach* are two of the most difficult organs to segment since *gallbladder* is very small and boundaries between *gallbladder* and *liver* are blurred while *stomach* has a significant intra-class variance. This reveals that our **MOSformer** can learn more discriminative features and have comprehensive understandings of organ structures.

Fig. 4 shows qualitative comparisons of **MOSformer** against several models on representative examples on the Synapse dataset. Most baselines suffer from segmentation target incompleteness (*e.g.*, *stomach*), misclassification of organs (*e.g.*, *spleen*), and blurry category boundaries (*e.g.*, *gallblad-*

Table 2: Comparison with the state-of-the-art models on the automated cardiac diagnosis challenge (ACDC) dataset. The best results are highlighted in **blue** and the second-best results are highlighted in **red**. We only report DSC in this table, following the evaluation setting of TransUNet [18]. Moreover, DSC of each anatomical structure is reported in this table. [†] means the results are borrowed from [40]. * means the baselines are implemented by ourselves.

Dimension	Method	Average DSC (%) \uparrow	RV	Myo	LV
2D	UNet [8] [MICCAI'15]	87.60	84.62	84.52	93.68
	AttnUNet [48] [MedIA'19]	86.90	83.27	84.33	93.53
	TransUNet [18] [MedIA'24]	89.71	86.67	87.27	95.18
	MISSFormer [37] [TMI'23]	91.19	89.85	88.38	95.34
	SwinUNet [17] [ECCVW'22]	88.07	85.77	84.42	94.03
	MT-UNet [49] [ICASSP'22]	90.43	86.64	89.04	95.62
	UCTransNet* [50] [AAAI'22]	91.98	90.06	89.87	96.02
3D	HiFormer* [51] [WACV'23]	90.40	88.24	87.63	95.30
	UNETR [†] [38] [WACV'22]	88.61	85.29	86.52	94.02
2.5D	nnFormer [40] [TIP'23]	92.06	90.94	89.58	95.65
	CAT-Net* [23] [TMI'22]	90.02	86.05	88.75	95.27
	MOSFormer [Ours]	92.19	90.86	89.65	96.05

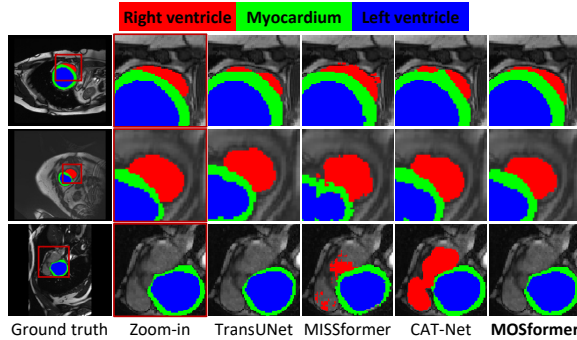


Figure 5: Visual comparisons with current state-of-the-art methods on the automatic cardiac diagnosis challenge (ACDC) dataset.

der), while **MOSFormer** can locate organs precisely, reduce the number of false positive predictions, and produce sharper boundaries.

Automated Cardiac Diagnosis Challenge (ACDC). To further prove model generalizing performance, **MOSFormer** is evaluated on the automated cardiac diagnosis challenge (ACDC) dataset. It should be noted that MRI images in this dataset can be considered anisotropic since they have high in-plane image resolution (*e.g.*, 1.37 \sim 1.68 mm) and low throughplane resolution (*e.g.*, 5 mm) [46]. Quantitative results are summarized in Table 2. Compared with state-of-the-art methods (2D, 2.5D, and 3D-based), **MOSFormer** achieves the best performance with 92.19% DSC. Thus, the above results indicate that our 2.5D-based **MOSFormer** is more advantageous to process anisotropic data compared with 3D-based models. Fig. 5 presents qualitative comparisons for different methods on this dataset. As seen, **MOSFormer** can locate anatomical structures more accurately. Specifically, in case 3, many models mistakenly classify regions outside the *myocardium* into the *right ventricle*

Table 3: Comparison with the state-of-the-art models on the abdominal organ segmentation (AMOS) dataset. The best results are highlighted in **blue** and the second-best results are highlighted in **red**. DSC is utilized as evaluation metric. Moreover, DSC of each organ is reported in this table. * means the baselines are implemented by ourselves.

Dimension	Method	Average DSC (%) \uparrow	Spleen	Kid. (R)	Kid. (L)	Gall.	Eso.	Liver	Stom.	Aotra	IVC	Panc.	Adr. (R)	Adr. (L)	Duo.	Blad.	Pros.
2D	UNet* [8] [MICCAI'18]	82.53	92.25	92.45	92.50	81.85	79.98	94.73	84.80	92.20	82.94	77.35	67.13	69.34	72.77	82.40	75.31
	TransUNet* [18] [MedIA'24]	80.10	91.26	92.47	91.90	78.01	77.00	94.93	80.04	91.98	82.99	74.30	63.66	53.84	71.65	81.37	76.03
	MISSFormer* [37] [TMIC'23]	78.16	93.13	91.98	91.88	75.89	71.87	94.27	80.14	88.74	77.53	71.39	60.65	59.32	64.43	77.97	73.16
	UCTransNet* [50] [AAAI'22]	82.34	93.37	92.32	91.90	77.09	79.77	94.78	85.95	91.77	82.84	77.44	65.88	68.98	71.36	83.93	77.71
	HiFormer* [51] [WACV'22]	80.03	92.73	92.79	92.01	79.44	76.42	94.55	82.65	90.56	80.16	73.59	61.14	58.73	68.12	82.01	75.64
3D	UNETR* [38] [WACV'22]	78.07	93.38	93.00	92.28	73.17	69.72	94.86	73.25	90.82	80.20	73.44	65.19	60.69	65.46	74.10	71.49
	nnFormer* [40] [TPR'23]	78.66	91.43	92.39	92.08	76.74	69.16	94.95	84.84	89.53	82.06	75.91	62.56	60.36	68.50	74.74	64.61
2.5D	MOSformer [Ours]	85.43	95.26	94.68	94.54	81.53	82.05	96.55	89.07	92.81	86.16	80.28	73.28	73.19	75.05	86.92	80.05

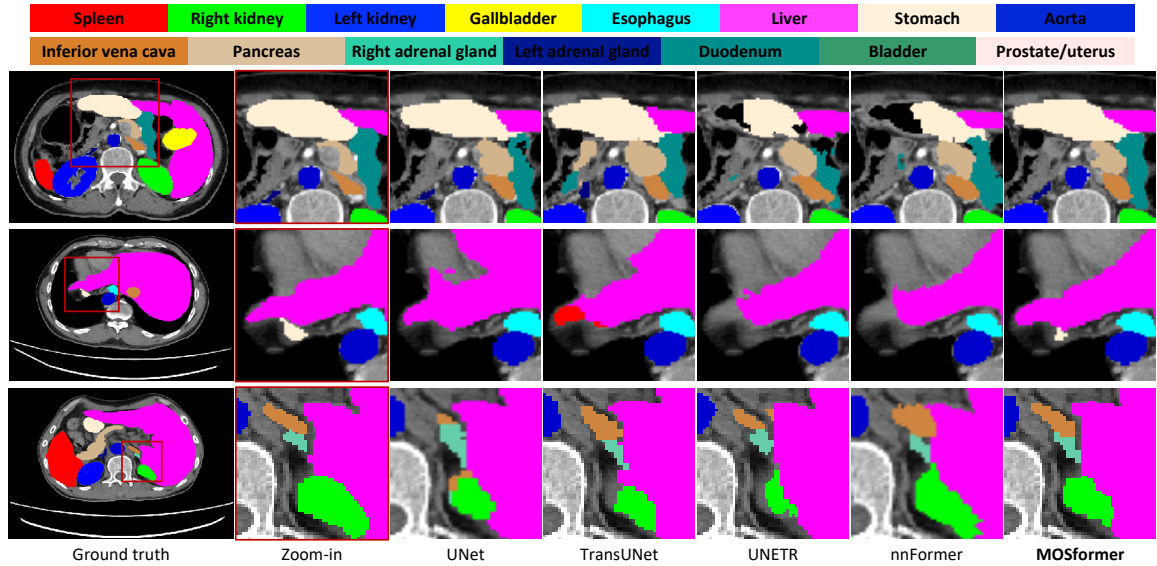


Figure 6: Visual comparisons with current state-of-the-art methods on the abdominal organ segmentation (AMOS) dataset.

while **MOSformer** donot produce any false positive predictions.

Abdominal Organ Segmentation (AMOS). Additionally, a large dataset with 200 training cases and 100 testing cases is also adopted in our experiments. Overall results and individual DSC on 15 organs are reported, as shown in Table 3. Our **MOSformer** achieves the best DSC in 14 organs and the second-best DSC in one organ. In a surprise, **MOSformer** offers 6.77% DSC improvement over 3D-based **nnFormer** while they have close performance on the multi-organ segmentation (Synapse) dataset. Based on the above observation, it can be concluded that the performance of **MOSformer** is more stable across different datasets compared with **nnFormer**. Visualization results are shown in Fig. 6. Compared with baselines, our **MOSformer** is able to accurately segment organs of diverse shapes and sizes, thus providing more consistent results with ground truth.

Table 4: Ablation studies of each component on the multi-organ segmentation (Synapse) and the automated cardiac diagnosis challenge (ACDC) datasets. Enc-S: Single encoder; Enc-D: Dual encoders; Enc-DM: Dual encoders with a momentum update. The best results are highlighted in **bold**. \dagger means the model is 2D-based.

Model	Module				Synapse	ACDC
	Enc-S	Enc-D	Enc-DM	IF-Trans	DSC (%) \uparrow	DSC (%) \uparrow
Model-1 \dagger	✓				82.42 (-3.21)	91.61 (-0.58)
Model-2	✓			✓	84.23 (-1.40)	92.04 (-0.15)
Model-3		✓		✓	84.93 (-0.70)	92.10 (-0.09)
MOSformer			✓	✓	85.63	92.19

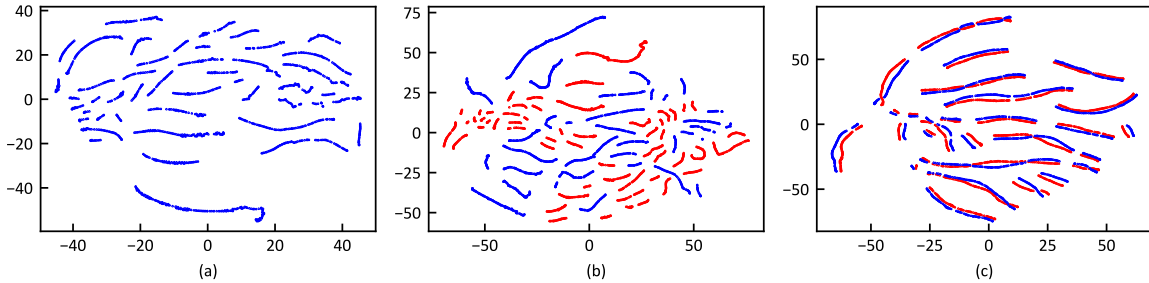


Figure 7: Visualization of embedding space learned under three encoder settings on the multi-organ segmentation (Synapse) *test* set. Distinct colors are used to differentiate embeddings from different encoders. Dimensions are reduced by t-SNE [55]. (a) Model-2 (Single encoder); (b) Model-3 (Dual encoders updated independently); (c) MOSformer (Dual encoders with a momentum update).

5.2 Ablation Study

Extensive ablation studies are conducted on the multi-organ segmentation (Synapse) and the automated cardiac diagnosis challenge (ACDC) datasets to verify the effectiveness of the momentum encoder and IF-Trans. DSC is selected as the default evaluation metric. Quantitative results are shown in Table 4. It should be noted that the baseline, Model-1, is a 2D-based model.

Importance of The Momentum Update. Two variants of **MOSformer** are employed in this experiment: **i)** Model-2: the encoder with a momentum update is removed, using a single encoder to extract features of target and neighborhood slices; **ii)** Model-3: the momentum encoder is replaced by a normal encoder and parameters of two encoders are updated independently via back-propagation. From quantitative results presented in Table 4, we can observe that these variants lead to decreased performance on both the Synapse dataset (1.40% and 0.70% in DSC) and the ACDC dataset (0.15% and 0.09% in DSC). The above results confirm the importance of the momentum update, designed to make slice features distinguishable and consistent. This design enables the model to distinguish target slices and fuse inter-slice information effectively.

Furthermore, we also adopt t-SNE [55] to visualize the encoded embedding space learned from three encoder settings on the multi-organ segmentation (Synapse) *test* set. Model-2 employs a single encoder to process all input slices, where all slice features originate from the same feature space, as depicted in Fig. 7 (a). This setup poses challenges for the model in distinguishing individual

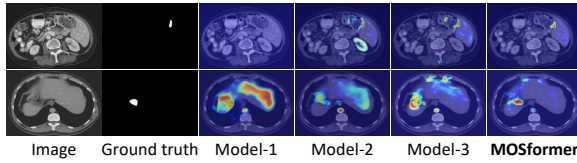


Figure 8: Class activation maps of the *gallbladder* and the *stomach* category (from top to bottom) produced by Grad-CAM [56]. The class activation maps are generated from the last decoder layer.

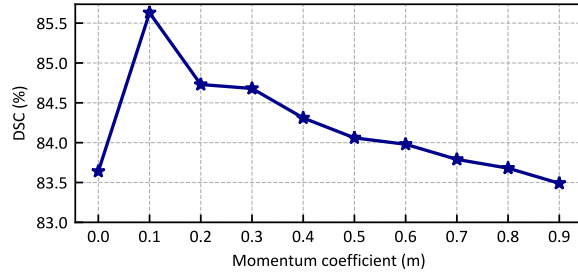


Figure 9: Effect of momentum coefficient m . We report DSC of **MOSformer** on the multi-organ segmentation (Synapse) dataset.

slices and acquiring slice-specific information during inter-slice fusion. In contrast, the embedding space learned by dual encoders is distinguishable, as illustrated in Fig. 7 (b) and (c). It can also be discovered that incorporating the momentum update in dual encoders facilitates consistency among slice features, as shown in Fig. 7 (c), thereby further boosting segmentation performance.

Efficacy of The Inter-slice Fusion Transformer. We remove IF-Trans modules in **MOSformer** and obtain a baseline model (**Model-1**). Compared with the baseline model, models incorporating IF-Trans (**Model-2** and **MOSformer**) offer substantial improvements on the Synapse (1.81% and 3.21% DSC gains) and the ACDC dataset (0.43% and 0.58% DSC gains). These results demonstrate inter-slice information is crucial in 3D medical image segmentation and the proposed IF-Trans can effectively fuse such information.

Additionally, we employ Grad-CAM [56] to visualize discriminative regions of the models, as depicted in Fig. 8. Compared with baseline **Model-1**, we can see that inter-slice information is beneficial, but **Model-2** and **Model-3** still tend to assign weights to irrelevant regions. Distinguishable and consistent inter-slice features within **MOSformer** can address the above issue, demonstrating enhanced precision in localizing organs of interest.

5.3 Hyperparameter Analysis

In this section, we conduct extensive analysis of several factors that correlate to segmentation performance of **MOSformer**. Default configurations of **MOSformer** are highlighted in gray.

Momentum Coefficient. The momentum coefficient, as described in Eq. (1), is an important hyperparameter in our model. We carry out detailed analysis on how m affects the model performance, as shown in Fig. 9. Our empirical observations indicate a consistent decline in model performance with incremental increases in m . This suggests that maintaining feature consistency

Table 5: Effect of neighborhood slice number s on the multi-organ segmentation (Synapse) and the automatic cardiac diagnosis challenge (ACDC) datasets. The best results are highlighted in **bold**.

Number	Synapse		ACDC	
	DSC (%) \uparrow	HD95 (mm) \downarrow	DSC (%) \uparrow	HD95 (mm) \downarrow
$s = 0$	83.73 (-1.90)	18.59 (+5.19)	91.71 (-0.48)	1.64 (+0.56)
$s = 1$	85.63	13.40	92.19	1.08
$s = 2$	84.95 (-0.68)	16.78 (+3.38)	91.91 (-0.28)	1.16 (+0.08)

Table 6: Effect of multi-scale inter-slice fusion on the multi-organ segmentation (Synapse) and the automatic cardiac diagnosis challenge (ACDC) datasets. The best results are highlighted in **bold**.

Scale	Synapse		ACDC	
	DSC (%) \uparrow	HD95 (mm) \downarrow	DSC (%) \uparrow	HD95 (mm) \downarrow
/16	83.00 (-2.63)	21.54 (+8.14)	91.63 (-0.56)	1.14 (+0.06)
/8, /16	83.76 (-1.87)	20.73 (+7.33)	91.75 (-0.44)	1.08 (+0.00)
/4, /8, /16	84.52 (-1.11)	15.81 (+2.41)	91.94 (-0.25)	1.08 (+0.00)
/2, /4, /8, /16	85.63	13.40	92.19	1.08

achieved through a relatively low momentum coefficient is advantageous. Specifically, a high momentum value (e.g., $m = 0.9$) leads to a significant drop in segmentation performance, from 85.63% to 83.49% in DSC. At the extreme case of no momentum ($m = 0$), the performance is nearly the poorest. These findings reinforce our motivation for extracting distinguishable and consistent slice features.

Neighborhood Slice Number. Since the proposed **MOSformer** is a 2.5D-based model, it requires neighborhood slices as additional inputs, as illustrated in Section 3. Thus, the number of neighborhood slices (s) is an important hyperparameter. Table 5 reports quantitative results for three different s parameters. It can be observed that segmentation performance initially increases and then decreases with an increasing value of s . Evidently, information from inter-slice enables our model to perceive partial structures of 3D medical volumes. However, a peculiar phenomenon emerges: segmentation performance of the model with $s = 2$ are worse than that with $s = 1$. Similar observations have been reported in [13]. One possible explanation is that the most valuable inter-slice information is derived from adjacent slices. Introducing non-adjacent slices may bring redundant information, which contributes negatively to model performance. Additionally, as s increases, the computational costs of our model also escalate. Based on the above observations, $s = 1$ is the most practical choice for our model.

Multi-scale Inter-slice Fusion. Multi-scale learning enables deep models to capture global spatial information and local contextual details. This conclusion has been supported by many studies [18], [17], [36]. In this paper, we further investigate multi-scale learning by incorporating inter-slice fusion. Table 6 presents results derived from four different inter-slice fusion configurations. Our default model achieves significant performance improvements, such as 1.11% \sim 2.63% gains in

Table 7: Model parameters, floating-point operations per second (FLOPs), and the average time required for segmenting individual cases. The input size of 2(.5)D-based and 3D-based models are set to 224×224 and $96 \times 96 \times 96$, respectively. * means the experiments are conducted on the *test* set of the multi-organ segmentation (Synapse) dataset and repeated five times.

Dimension	Method	#params (M)	FLOPs (G)	Time* (s)
2D	UNet [8] [MICCAI'15]	17.26	30.74	0.67
	TransUNet [18] [MedIA'24]	93.23	24.73	5.69
	MISSformer [37] [TMI'23]	35.45	7.28	7.20
3D	UNETR [38] [WACV'22]	92.62	82.63	5.39
	nnFormer [40] [TIP'23]	149.13	246.10	10.13
2.5D	CAT-Net [23] [TMI'22]	220.16	121.83	21.34
	MOSformer [Ours]	77.09	100.06	5.10

DSC on the multiorgan segmentation (Synapse) dataset and $0.25\% \sim 0.56\%$ gains in DSC on the automatic cardiac diagnosis (ACDC) dataset. With more scales of inter-slice information fused, **MOSformer** demonstrates an enhanced ability to comprehend global shapes and anatomical details within segmentation targets. This enhancement facilitates precise localization of semantic regions, resulting in higher DSC, and accurate classification of category boundaries, reflected in smaller HD95.

5.4 Model Complexity

Table 7 presents a comparison of five medical image segmentation models with **MOSformer** across various dimensions, including model parameters, floating-point operations per second (FLOPs), and the average time required for segmenting individual cases. **MOSformer** maintains a relatively small size (77.09 M) compared with 3D-based and 2.5D-based models. Furthermore, **MOSformer** exhibits an inference speed only half that of **nnFormer** [40], even surpassing 2D-based **TransUNet** [18] and **MISSformer** [37]. These results indicate **MOSformer** can achieve a favorable trade-off between model complexity and segmentation performance.

6 Conclusion

This paper proposes a **M**omentum encoder-based **I**nter-**S**lice fusion **T**rans**F**ormer (**MOSformer**) for stable and precise medical image segmentation. Dual encoders with a momentum update are able to guarantee both feature distinguishability and consistency, beneficial for inter-slice fusion. Besides, rich contexts can be captured via inter-slice self-attention in the IF-Trans module. The superior performance to state-of-the-arts on three benchmarks has demonstrated the **MOSformer**'s effectiveness and competitiveness. It will be extended to other downstream medical analysis tasks in our subsequent works.

Acknowledgments

Funding

This work was supported in part by the National Key Research and Development Program of China under Grant 2023YFC2415100, in part by the National Natural Science Foundation of China under Grant 62222316, Grant 62373351, Grant 82327801, Grant 62073325, Grant 62303463, in part by the Chinese Academy of Sciences Project for Young Scientists in Basic Research under Grant No. YSBR-104, in part by the Beijing Natural Science Foundation under Grant F252068, Grant 4254107, in part by China Postdoctoral Science Foundation under Grant 2024M763535 and in part by CAMS Innovation Fund for Medical Sciences (CIFMS) under Grant 2023-I2M-C&T-B-017.

Author Contributions

D.X. Huang performed data curation, developed the methodology, conducted the experiments, and drafted the original manuscript. X.H. Zhou conceived the study and acquired funding, with additional funding support from M.J. Gui. X.L. Xie, S.Q. Liu, S.Y. Wang, and Z.Q. Feng reviewed and edited the manuscript. Z.G. Hou supervised the project. All authors approved the final version of the manuscript.

Conflicts of Interest

The authors declare that there is no conflict of interest regarding the publication of this article.

Data Availability

Data will be made available on reasonable request.

References

1. Antonelli M, Reinke A, Bakas S, et al. The medical segmentation decathlon. *Nature Communications* 2022;13:4128.
2. Han Z, Tian H, Han X, et al. A respiratory motion prediction method based on LSTM-AE with attention mechanism for spine surgery. *Cyborg and Bionic Systems* 2024;5:0063.
3. Huang DX, Zhou XH, Xie XL, et al. Real-time 2D/3D registration via CNN regression and centroid alignment. *IEEE Transactions on Automation Science and Engineering* 2025;22:85–98.
4. Chen Y, Li G, Li C, et al. GVM-Net: A GNN-based vessel matching network for 2D/3D non-rigid coronary artery registration. *IEEE Transactions on Medical Imaging* 2025. DOI: [10.1109/TMI.2025.3540906](https://doi.org/10.1109/TMI.2025.3540906).
5. Zhang J, Liu L, Xiang P, et al. AI co-pilot bronchoscope robot. *Nature Communications* 2024;15:241.

6. Li L, Li X, Ouyang B, Mo H, Ren H, and Yang S. Three-dimensional collision avoidance method for robot-assisted minimally invasive surgery. *Cyborg and Bionic Systems* 2023;4:0042.
7. Zhou XH, Xie XL, Liu SQ, et al. Learning skill characteristics from manipulations. *IEEE Transactions on Neural Networks and Learning Systems* 2023;34:9727–41.
8. Ronneberger O, Fischer P, and Brox T. U-Net: Convolutional networks for biomedical image segmentation. In: *Proceedings of the International Conference on Medical Image Computing and Computer Assisted Interventions (MICCAI)*. 2015:234–41.
9. Zhou Z, Siddiquee MMR, Tajbakhsh N, and Liang J. UNet++: Redesigning skip connections to exploit multiscale features in image segmentation. *IEEE Transactions Medical Imaging* 2019;39:1856–67.
10. Huang H, Lin L, Tong R, et al. UNet 3+: A full-scale connected UNet for medical image segmentation. In: *Proceedings of the IEEE International Conference on Acoustics, Speech and Signal Processing (ICASSP)*. 2020:1055–9.
11. Huang DX, Zhou XH, Xie XL, et al. SPIRONet: Spatial-frequency learning and topological channel interaction network for vessel segmentation. [arXiv:2406.19749](https://arxiv.org/abs/2406.19749) 2024.
12. Tajbakhsh N, Jeyaseelan L, Li Q, Chiang JN, Wu Z, and Ding X. Embracing imperfect datasets: A review of deep learning solutions for medical image segmentation. *Medical Image Analysis* 2020;63:101693.
13. Zhang Y, Liao Q, Ding L, and Zhang J. Bridging 2D and 3D segmentation networks for computation-efficient volumetric medical image segmentation: An empirical study of 2.5D solutions. *Computerized Medical Imaging and Graphics* 2022;102088.
14. Azad R, Aghdam EK, Rauland A, et al. Medical image segmentation review: The success of U-Net. *IEEE Transactions on Pattern Analysis and Machine Intelligence* 2024;46:10076–95.
15. Mou L, Zhao Y, Fu H, et al. CS²-Net: Deep learning segmentation of curvilinear structures in medical imaging. *Medical Image Analysis* 2021;67:101874.
16. Roy K, Banik D, Bhattacharjee D, Krejcar O, and Kollmann C. LwMLA-NET: A lightweight multi-level attention-based network for segmentation of COVID-19 lungs abnormalities from CT images. *IEEE Transactions on Instrumentation and Measurement* 2022;71:5007813.
17. Cao H, Wang Y, Chen J, et al. Swin-UNet: Unet-like pure transformer for medical image segmentation. In: *Proceedings of the European Conference on Computer Vision Workshops (ECCVW)*. 2022:205–18.
18. Chen J, Mei J, Li X, et al. TransUNet: Rethinking the U-Net architecture design for medical image segmentation through the lens of transformers. *Medical Image Analysis* 2024;97:103280.
19. Çiçek Ö, Abdulkadir A, Lienkamp SS, Brox T, and Ronneberger O. 3D U-Net: learning dense volumetric segmentation from sparse annotation. In: *Proceedings of the International Conference on Medical Image Computing and Computer Assisted Interventions (MICCAI)*. 2016:424–32.

20. Yu L, Cheng JZ, Dou Q, et al. Automatic 3D cardiovascular MR segmentation with densely-connected volumetric convnets. In: *Proceedings of the International Conference on Medical Image Computing and Computer Assisted Interventions (MICCAI)*. 2017:287–95.
21. Chen J, Yang L, Zhang Y, Alber M, and Chen DZ. Combining fully convolutional and recurrent neural networks for 3D biomedical image segmentation. In: *Proceedings of the Advances in Neural Information Processing Systems (NeurIPS)*. Vol. 29. 2016.
22. Yan X, Tang H, Sun S, Ma H, Kong D, and Xie X. AFTer-UNet: Axial fusion transformer UNet for medical image segmentation. In: *Proceedings of the IEEE/CVF Winter Conference on Applications of Computer Vision (WACV)*. 2022:3971–81.
23. Hung ALY, Zheng H, Miao Q, Raman SS, Terzopoulos D, and Sung K. CAT-Net: A cross-slice attention transformer model for prostate zonal segmentation in MRI. *IEEE Transactions Medical Imaging* 2022;42:291–303.
24. Zhang Y, Yuan L, Wang Y, and Zhang J. SAU-Net: Efficient 3D spine MRI segmentation using inter-slice attention. In: *Proceedings of the Medical Imaging With Deep Learning (MIDL)*. 2020:903–13.
25. Liu Z, Lin Y, Cao Y, et al. Swin Transformer: Hierarchical vision transformer using shifted windows. In: *Proceedings of the IEEE/CVF International Conference on Computer Vision (ICCV)*. 2021:10012–22.
26. Yu Q, Xie L, Wang Y, Zhou Y, Fishman EK, and Yuille AL. Recurrent saliency transformation network: Incorporating multi-stage visual cues for small organ segmentation. In: *Proceedings of the IEEE/CVF Conference on Computer Vision and Pattern Recognition (CVPR)*. 2018:8280–9.
27. Li Y, Li H, and Fan Y. ACEnet: Anatomical context-encoding network for neuroanatomy segmentation. *Medical Image Analysis* 2021;70:101991.
28. Yang X, Yu L, Li S, et al. Towards automated semantic segmentation in prenatal volumetric ultrasound. *IEEE Transactions Medical Imaging* 2018;38:180–93.
29. Pang B, Zha K, Cao H, Shi C, and Lu C. Deep RNN framework for visual sequential applications. In: *Proceedings of the IEEE/CVF Conference on Computer Vision and Pattern Recognition (CVPR)*. 2019:423–32.
30. Li L, Lian S, Luo Z, Li S, Wang B, and Li S. Learning consistency-and discrepancy-context for 2D organ segmentation. In: *Proceedings of the International Conference on Medical Image Computing and Computer Assisted Interventions (MICCAI)*. 2021:261–70.
31. Guo D and Terzopoulos D. A transformer-based network for anisotropic 3D medical image segmentation. In: *Proceedings of the IEEE International Conference on Image Processing (ICIP)*. 2021:8857–61.
32. Hung ALY, Zheng H, Zhao K, et al. CSAM: A 2.5 D cross-slice attention module for anisotropic volumetric medical image segmentation. In: *Proceedings of the IEEE/CVF Winter Conference on Applications of Computer Vision (WACV)*. 2024:5923–32.

33. Dosovitskiy A, Beyer L, Kolesnikov A, et al. An image is worth 16x16 words: Transformers for image recognition at scale. In: *Proceedings of the International Conference on Learning Representations (ICLR)*. 2020.
34. Carion N, Massa F, Synnaeve G, Usunier N, Kirillov A, and Zagoruyko S. End-to-end object detection with transformers. In: *Proceedings of the European Conference on Computer Vision (ECCV)*. 2020:213–29.
35. Lijin P, Ullah M, Vats A, Cheikh FA, Nair MS, et al. Dual encoder decoder shifted window-based transformer network for polyp segmentation with self-learning approach. *IEEE Transactions on Artificial Intelligence* 2024;5:3456–69.
36. Chenyu Y, Zhao R, Liu F, et al. Class-aware generative adversarial transformers for medical image segmentation. In: *Proceedings of the Advances in Neural Information Processing Systems (NeurIPS)*. 2022.
37. Huang X, Deng Z, Li D, Yuan X, and Fu Y. MISSFormer: An effective rransformer for 2D medical image segmentation. *IEEE Transactions Medical Imaging* 2023;42:1484–94.
38. Hatamizadeh A et al. UNETR: Transformers for 3D medical image segmentation. In: *Proceedings of the IEEE/CVF Winter Conference on Applications of Computer Vision (WACV)*. 2022:574–84.
39. Xie Y, Zhang J, Shen C, and Xia Y. CoTr: Efficiently bridging cnn and transformer for 3D medical image segmentation. In: *Proceedings of the International Conference on Medical Image Computing and Computer Assisted Interventions (MICCAI)*. 2021:171–80.
40. Zhou HY et al. nnFormer: Volumetric medical image segmentation via a 3D transformer. *IEEE Transactions Image Processing* 2023;32:4036–45.
41. He K, Zhang X, Ren S, and Sun J. Deep residual learning for image recognition. In: *Proceedings of the IEEE/CVF Conference on Computer Vision and Pattern Recognition (CVPR)*. 2016:770–8.
42. He K, Fan H, Wu Y, Xie S, and Girshick R. Momentum contrast for unsupervised visual representation learning. In: *Proceedings of the IEEE/CVF Conference on Computer Vision and Pattern Recognition (CVPR)*. 2020:9729–38.
43. Vaswani A, Shazeer N, Parmar N, et al. Attention is all you need. In: *Proceedings of the Advances in Neural Information Processing Systems (NeurIPS)*. Vol. 30. 2017.
44. Lee CY, Xie S, Gallagher P, Zhang Z, and Tu Z. Deeply-supervised nets. In: *Proceedings of the International Conference on Artificial Intelligence and Statistics (AISTATS)*. 2015:562–70.
45. Landman B, Xu Z, Iglesias J, Styner M, Langerak T, and Klein A. MICCAI multi-atlas labeling beyond the cranial vault–workshop and challenge. In: *Proceedings of the International Conference on Medical Image Computing and Computer Assisted Interventions Workshops (MICCAIW)*. Vol. 5. 2015:12.

46. Bernard O et al. Deep learning techniques for automatic MRI cardiac multi-structures segmentation and diagnosis: Is the problem solved? *IEEE Transactions Medical Imaging* 2018;37:2514–25.
47. Ji Y, Bai H, Ge C, et al. AMOS: A large-scale abdominal multi-organ benchmark for versatile medical image segmentation. In: *Proceedings of the Advances in Neural Information Processing Systems (NeurIPS)*. Vol. 35. 2022:36722–32.
48. Schlemper J, Oktay O, Schaap M, et al. Attention gated networks: Learning to leverage salient regions in medical images. *Medical Image Analysis* 2019;53:197–207.
49. Wang H, Xie S, Lin L, et al. Mixed transformer U-Net for medical image segmentation. In: *Proceedings of the IEEE International Conference on Acoustics, Speech and Signal Processing (ICASSP)*. 2022:2390–4.
50. Wang H, Cao P, Wang J, and Zaiane OR. UCTransNet: Rethinking the skip connections in U-Net from a channel-wise perspective with transformer. In: *Proceedings of the AAAI Conference on Artificial Intelligence (AAAI)*. Vol. 36. 3. 2022:2441–9.
51. Heidari M, Kazerouni A, Soltany M, et al. HiFormer: Hierarchical multi-scale representations using transformers for medical image segmentation. In: *Proceedings of the IEEE/CVF Winter Conference on Applications of Computer Vision (WACV)*. 2023:6202–12.
52. Milletari F, Navab N, and Ahmadi SA. V-Net: Fully convolutional neural networks for volumetric medical image segmentation. In: *Proceedings of the International Conference on 3D Vision (3DV)*. 2016:565–71.
53. Hatamizadeh A, Nath V, Tang Y, Yang D, Roth HR, and Xu D. Swin UNETR: Swin transformers for semantic segmentation of brain tumors in MRI images. In: *Proceedings of the International Conference on Medical Image Computing and Computer Assisted Interventions Workshops (MICCAIW)*. 2021:272–84.
54. Zhang W, Zhang Y, and Zhang L. Multi-planar data augmentation and lightweight skip connection design for deep learning based abdominal CT image segmentation. *IEEE Transactions on Instrumentation and Measurement* 2023;72:2532111.
55. Van der Maaten L and Hinton G. Visualizing data using t-SNE. *Journal of Machine Learning Research* 2008;9.
56. Selvaraju RR, Cogswell M, Das A, Vedantam R, Parikh D, and Batra D. Grad-CAM: Visual explanations from deep networks via gradient-based localization. In: *Proceedings of the IEEE/CVF International Conference on Computer Vision (ICCV)*. 2017:618–26.